



The Chemistry of Phosphorus-bearing Molecules under Energetic Phenomena

Izaskun Jiménez-Serra¹, Serena Viti², David Quénard¹, and Jonathan Holdship²¹ School of Physics & Astronomy, Queen Mary University of London, Mile End Road, E1 4NS, London, UK; i.jimenez-serra@qmul.ac.uk² Department of Physics & Astronomy, University College London, Gower Street London, WC1E 6BT, London, UK

Received 2018 February 26; revised 2018 June 16; accepted 2018 June 18; published 2018 July 31

Abstract

For decades, the detection of phosphorus-bearing molecules in the interstellar medium was restricted to high-mass star-forming regions (e.g., SgrB2 and Orion KL) and the circumstellar envelopes of evolved stars. However, recent higher-sensitivity observations have revealed that molecules such as PN and PO are present not only toward cold massive cores and low-mass star-forming regions with PO/PN ratios ≥ 1 but also toward the giant molecular clouds in the Galactic center known to be exposed to highly energetic phenomena such as intense UV radiation fields, shock waves, and cosmic rays. In this paper, we carry out a comprehensive study of the chemistry of phosphorus-bearing molecules across different astrophysical environments that cover a range of physical conditions (cold molecular dark clouds, warm clouds, and hot cores/hot corinos) and are exposed to different physical processes and energetic phenomena (proto-stellar heating, shock waves, intense UV radiation, and cosmic rays). We show how the measured PO/PN ratio (either ≥ 1 , as in, e.g., hot molecular cores, or ≤ 1 , as in UV strongly illuminated environments) can provide constraints on the physical conditions and energetic processing of the source. We propose that the reaction $P + OH \rightarrow PO + H$, not included in previous works, could be an efficient gas-phase PO formation route in shocks. Our modeling provides a template with which to study the detectability of P-bearing species not only in regions in our own Galaxy but also in extragalactic sources.

Key words: astrochemistry – ISM: molecules – methods: numerical

1. Introduction

Phosphorus is considered one of the main biogenic elements due to its key role in biochemical processes in living organisms (Maciá 2005). Phosphorus is believed to be synthesized in massive stars and subsequently ejected into the interstellar medium (ISM) by supernova explosions (Koo et al. 2013). Although its cosmic abundance is relatively high (fractional abundance of $\sim 3 \times 10^{-7}$ with respect to H; Asplund et al. 2009), it is difficult to detect in the ISM, since it is likely to be heavily depleted onto dust grains (see Turner et al. 1990).

Indeed, phosphorus-bearing (hereafter P-bearing) species have mainly been detected toward diffuse clouds (in the form of P^+ ; Jura & York 1978) and circumstellar envelopes around evolved stars (in the form of HCP, CP, CCP, NCCP, PO, PN, and PH_3 ; Agúndez et al. 2007, 2008, 2014a, 2014b; Tenenbaum et al. 2007; Halfen et al. 2008; Milam et al. 2008; Tenenbaum & Ziurys 2008; De Beck et al. 2013). More recently, higher-sensitivity observations have revealed the presence of P-bearing molecules such as PN and PO in regions with active low-mass and high-mass star formation (Caux et al. 2011; Yamaguchi et al. 2011; Lefloch et al. 2016; Rivilla et al. 2016). Also, PN has been reported toward massive starless cores (Fontani et al. 2016), which suggests that this molecule could form in relatively quiescent and cold gas (Mininni et al. 2018). In all cases, PO seems to be slightly more abundant than PN (by factors of 2–3; see, e.g., Rivilla et al. 2016),³ and the PO/PN ratio can potentially be used as a length indicator of the pre-stellar collapse phase (see Aota & Aikawa 2012; Lefloch et al. 2016). The analysis of the P-bearing content of the giant molecular clouds (GMCs) in the

Galactic center shows that PN and PO can also be detected in molecular clouds subject to extreme conditions, such as those found in galactic nuclei (Rivilla et al. 2018).

The lack of many detections of P-bearing molecules has indeed hampered the study of the chemistry of these species in the ISM. Initial theoretical works focused on the chemistry of cold and warm molecular clouds (Millar 1991) and massive hot molecular cores (Charnley & Millar 1994). With the detection of P-bearing molecules in the circumstellar envelopes of evolved stars, more modeling was carried out by MacKay & Charnley (2001) and Agúndez et al. (2007), exploring the nonequilibrium chemistry of phosphorus in the outer envelope of these objects. The recent detections of PN and PO in star-forming regions has triggered a new interest in the chemistry of phosphorus in the ISM. While Yamaguchi et al. (2011) and Lefloch et al. (2016) proposed that P-bearing species are produced in shocked gas after the sputtering of dust grains, Rivilla et al. (2016) suggested that P-bearing molecules are formed during the cold collapse phase and subsequently frozen onto dust grains (Caux et al. 2011; Fontani et al. 2016; Rivilla et al. 2016). The detection of PN and PO in the Galactic center poses even more unknowns to the chemistry of phosphorus (Rivilla et al. 2018). These authors have indeed found a positive trend between the abundance of PN and the optically thin ^{29}SiO isotopologue, which suggests that PN is generated in shocks. However, it is unclear whether P-bearing molecules can survive additional energetic processing due to the intense UV radiation and/or enhanced cosmic rays known to be present in this region of the Galaxy.

In this paper, we present a comprehensive study of the chemistry of phosphorus in the ISM covering a wide range of physical conditions (from molecular dark clouds to cold/warm/hot cores) and processes (proto-stellar heating, shock waves, UV radiation, and cosmic rays). Our goal is to establish the most likely conditions under which P-bearing molecules form, and to what extent. Special focus is put on the analysis of

³ Note that these PO/PN ratios were estimated assuming local thermodynamic equilibrium (LTE) conditions. These ratios may vary once collisional rate coefficients become available for PO with He and/or H_2 (see Lique et al. 2018).

the PO/PN abundance ratio to determine why this ratio is found to be constant (within a factor of 2–3) across different sources. In Section 2, we describe the details of our chemical modeling, while in Section 3, we present the results. In Section 4, we discuss the implications of our modeling for Galactic and extragalactic studies, and we summarize our conclusions in Section 5.

2. Chemical Modeling of P-bearing Molecules

To model the chemistry of P-bearing species, we have used the gas-grain chemical code UCLCHEM (Holdship et al. 2017),⁴ which has been recently updated with a new treatment for the grain surface chemistry (Quénard et al. 2018). The code includes thermal and nonthermal desorption processes as described in Viti et al. (2004) and Roberts et al. (2007), respectively, and considers the grain surface processes of radical diffusion, chemical reactive desorption, and reaction-diffusion competition as described in Quénard et al. (2018).

The chemical network is based on the one developed by Quénard et al. (2018), which has been expanded to include P-bearing species. The gas-phase reactions were taken from the UMIST database (McElroy et al. 2013), which includes the original network for phosphorus of Millar (1991). This network is based on the early experimental work of Thorne et al. (1983, 1984) and Smith et al. (1989), and only $\sim 30\%$ of the reactions have rate coefficients measured in the laboratory. We have also added the chemical reactions involving PH_3 from the chemical network of Charney & Millar (1994), who took the rate coefficients of the neutral-neutral reactions $\text{H} + \text{PH}_n$ ($n = 1-3$) from Kaye & Strobel (1983) following the experimental data of Lee et al. (1976). Other ion-neutral reactions involving PH_n products and species such as PS or HPS were also included in our network following Anicich (1993) and according to the experiments of Smith et al. (1989). The two gas-phase reactions, $\text{N} + \text{CP} \rightarrow \text{PN} + \text{C}$ and $\text{P} + \text{CN} \rightarrow \text{PN} + \text{C}$, proposed by Agúndez et al. (2007) with reaction rates of $3 \times 10^{-10} \text{ cm}^3 \text{ s}^{-1}$ were also included in our network. Note that these reaction rates are highly uncertain, since no experimental values are available. However, several models were run without these reactions, and they yielded similar results.

For the grain surface chemistry, we have considered the hydrogenation reactions of P-bearing species into their nonsaturated and saturated forms, as well as their associated diffusion and chemical reaction desorption reactions. Binding energies were taken from the KIDA database (Wakelam et al. 2017).⁵ In total, the network contains 3695 reactions involving 401 species, 265 of which are gas-phase species, while the remaining 136 are grain surface species.

The initial elemental abundances considered in our models were taken from Asplund et al. (2009; see the solar values in their Table 1), except for Mg, Si, Cl, and F, which have been depleted by factors between 5.4 and 5700 (see Table 1 and references therein). For P, its elemental abundance has been depleted by a factor of 100 with respect to its solar value ($\text{P}/\text{H} = 2.57 \times 10^{-7}$) to simulate the fact that phosphorus is not detected in quiescent molecular clouds (Turner et al. 1990). Note that in the models of Aota & Aikawa (2012), a higher initial abundance of P/ PH_3 of $\sim 10^{-8}$ is also considered in the ices, which corresponds to a depletion factor of ~ 10 . However, a better agreement with the observations toward the B1

Table 1
Assumed Elemental Abundances with Respect to n_{H}

Element	Abundance	Reference
He	0.085	(1)
C	2.692×10^{-4}	(1)
O	4.898×10^{-4}	(1)
N	6.761×10^{-5}	(1)
S	1.318×10^{-5}	(1)
Mg	7.0×10^{-9}	(2)
Si	8.0×10^{-9}	(2)
Cl	1.58×10^{-9}	(3)
P	2.57×10^{-9}	(4)
F	6.7×10^{-9}	(5)

References. (1) Extracted from Asplund et al. (2009). (2) As in the low metal abundance case from Morton (1974) and Graedel et al. (1982). (3) Taken from Schilke et al. (1995), Cernicharo et al. (2010), and Codella et al. (2012). (4) As inferred by Lefloch et al. (2016). (5) As derived by Neufeld et al. (2005).

shocked region in the L1157 molecular outflow is obtained when this initial abundance is reduced to $\sim 3 \times 10^{-9}$ (see their Section 3.2). This is also supported by recent findings by Lefloch et al. (2016) and Rivilla et al. (2016) in, respectively, L1157-B1 and a sample of massive star-forming regions. Therefore, it is reasonable to assume that P is likely depleted by a factor of 100 in molecular dark clouds.

We run UCLCHEM in three phases. Phase 0 simulates the chemistry in a diffuse cloud with density $n(\text{H}) = 100 \text{ cm}^{-3}$ and temperature 20 K for 10^6 yr. We have also tested higher temperatures for the Phase 0 stage ($T = 100$ K; see Turner et al. 1999), and the abundances of the P-bearing species at the end of Phase 1 (the collapse phase; see below) differ by less than 10%. In Phase 1, the cloud undergoes freefall collapse, keeping the temperature constant at 10 K until the final density ($n(\text{H}) = 2 \times 10^4$, 2×10^5 , and $2 \times 10^6 \text{ cm}^{-3}$) is reached. As explained in Section 3.1, we have investigated the effects of a short-lived/long-lived collapse phase, since it has been found to have important implications for the chemistry of PN and PO (see, e.g., Aota & Aikawa 2012; Lefloch et al. 2016). Finally, Phase 2 simulates the physical processes associated with star formation, such as warm-up of the proto-stellar envelope (up to 50, 100, and 300 K, as described in Viti et al. 2004), interaction of C-type shocks (for shock velocities of $v_s = 20$ and 40 km s^{-1} and using the parameterization of the physical structure of C-shock waves formulated by Jiménez-Serra et al. 2008), intense UV radiation (with $\chi = 1, 10^2$, and 10^4 Habing, as explored in Viti & Williams 1999), and cosmic rays (with $\zeta = 1.3 \times 10^{-17}$, 1.3×10^{-15} , and $1.3 \times 10^{-13} \text{ s}^{-1}$; see Harada et al. 2015).

3. Results

3.1. Effects of Collapse on the Chemistry of P-bearing Species

In Figure 1, we show the results obtained for the collapse phase (Phase 1 in UCLCHEM) for final gas densities $n(\text{H}) = 2 \times 10^4$, 2×10^5 , and $2 \times 10^6 \text{ cm}^{-3}$ considering a short-lived collapse (the code stops once the final density is reached, i.e., at timescales of $5.2-5.4 \times 10^6$ yr, depending on the final density) and a long-lived collapse (chemistry runs until a final timescale of 6×10^6 yr, i.e., between 6 and 8×10^5 yr longer after the final density is attained; see also Table 2). In

⁴ <https://uclchem.github.io/>

⁵ <http://kida.obs.u-bordeaux1.fr/>

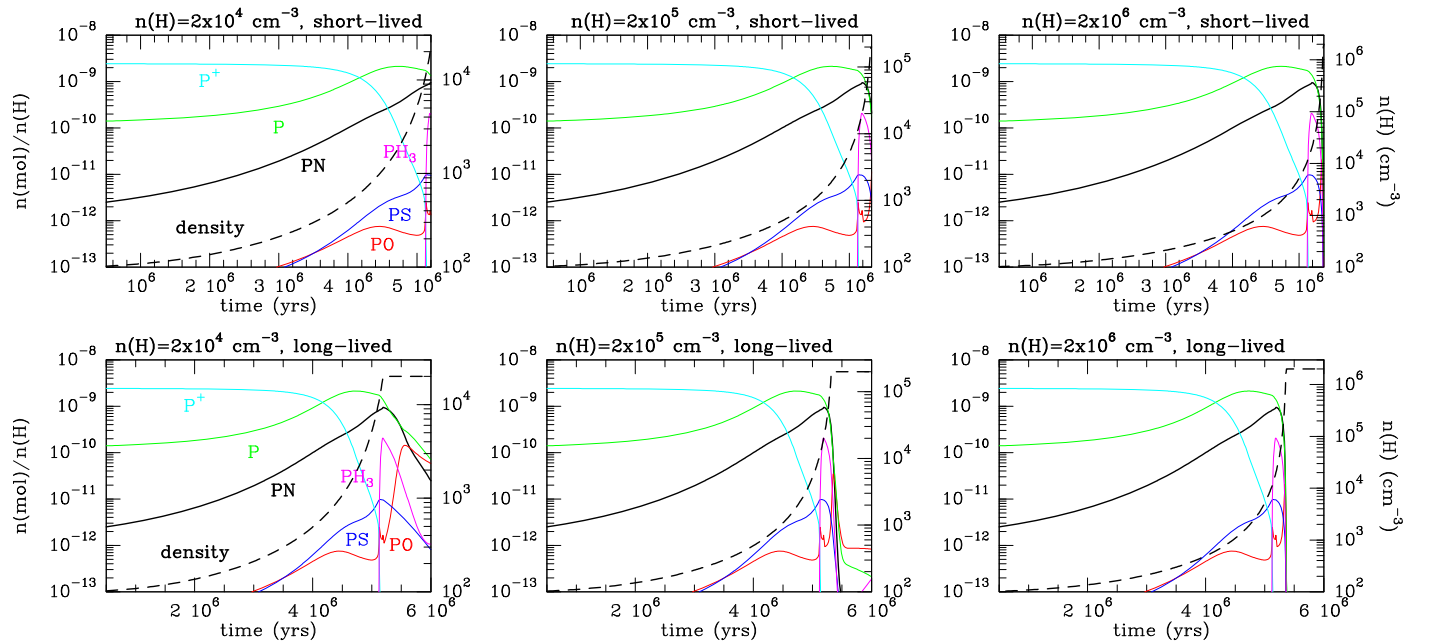


Figure 1. Abundances of P-bearing species as a function of time simulated during the freefall collapse of a cloud for final densities of $n(\text{H}) = 2 \times 10^4$ (left), 2×10^5 (middle), and 2×10^6 cm^{-3} (right). The length of the collapse is varied so that the chemistry stops when the final density is reached (short-lived collapse; upper panels) or is allowed to evolve for a few 10^5 yr more after the final density is reached (long-lived collapse; lower panels).

earlier works (see Aota & Aikawa 2012; Lefloch et al. 2016), the length of the collapse was found to have a strong impact on the subsequent evolution of the chemistry of PO and PN and their predicted abundance ratio. Indeed, in the short-lived scenario, the gas-phase abundance of atomic nitrogen by the end of the collapse is large, which enhances the formation of PN and yields PO/PN ratios ≤ 1 . On the contrary, if the collapse is long-lived, atomic nitrogen has enough time to deplete on grain surfaces and get converted mainly into NH_3 , giving as a result PO/PN ratios ≥ 1 (Lefloch et al. 2016). We therefore explore the consequences of the length of the collapse in our models by making the core become static for an extra $6\text{--}8 \times 10^5$ yr after the end of the collapse. This extra time is consistent with the estimated lower-limit dynamical age of pre-stellar cores ($\geq 1\text{--}2 \times 10^5$ yr; see Section 4 in Pagani et al. 2012) and provides a good match to observations toward this type of core (Quénard et al. 2018).

In our models, we assume a physical radius for the core of 0.3 pc, which implies visual extinctions of 13, 120, and 1200 mag for hydrogen densities of $n(\text{H}) = 2 \times 10^4$, 2×10^5 , and 2×10^6 cm^{-3} , respectively, according to the expression (Bohlin et al. 1978; Frerking et al. 1982)

$$A_v = A_{v0} + \frac{n(\text{H}) \times r_{\text{out}}}{1.6 \times 10^{21}} \text{ mag}, \quad (1)$$

where r_{out} is the radius of the core, $n(\text{H})$ is the number density of hydrogen nuclei, A_{v0} is the background extinction assumed to be 2 mag, and A_v is the total extinction within the core.

As shown in Figure 1, for all models, the most abundant P-bearing species during the collapse are atomic phosphorus (P) and PN, with maximum abundances of $\sim 5 \times 10^{-10}\text{--}10^{-9}$ at timescales of $\sim 5 \times 10^6$ yr (i.e., when the final density is reached). The formation of PN in detectable abundances starts with the

gas-phase reactions $\text{N} + \text{CP} \rightarrow \text{PN} + \text{C}$ and $\text{P} + \text{CN} \rightarrow \text{PN} + \text{C}$ and proceeds through the reaction $\text{N} + \text{PO} \rightarrow \text{PN} + \text{O}$ in the gas phase by the end of the collapse. The formation of PO and PS is delayed with respect to PN, and it occurs in the gas phase via reactions $\text{O} + \text{PH} \rightarrow \text{PO} + \text{H}$ and $\text{HPS}^+ + e^- \rightarrow \text{PS} + \text{H}$, respectively. PH_3 dramatically increases its gas-phase abundance by the end of the collapse when it is efficiently formed on grain surfaces via hydrogenation and subsequently nonthermally desorbed.

At the highest densities in the collapse, the gas-phase abundances of all P-bearing species start to decrease due to the freeze out onto dust grains. This depletion is more extreme in the long-lived case, since species can freeze out for longer, reaching gas-phase abundances even lower than 10^{-13} . Except for models with $n(\text{H}) = 2 \times 10^6$ cm^{-3} , where all P-bearing species are fully frozen out in both the long-lived and short-lived cases, these differences in depletion by the end of the collapse have an impact on the PO/PN abundance ratio predicted during Phase 2 (see Sections 3.2–3.5).

3.2. Effects of Proto-stellar Heating

In this section, we analyze the effects of the increase of dust and gas temperature due to the protostar on the chemistry of phosphorus. We consider a range of hydrogen gas densities ($n(\text{H}) = 2 \times 10^4$, 2×10^5 , and 2×10^6 cm^{-3}) and final temperatures ($T = 50$, 100, and 300 K) that are typically found in warm and hot cores (see Table 2). We simulate the effect of the presence of a protostar at the center of the core by subjecting it to an increase in the gas and dust temperature. The temperature reaches its maximum value at the contraction time of the core (occurring at timescales $\leq 10^5$ yr), following a power law derived by Viti et al. (2004) from the observational luminosity function of Molinari et al. (2000). For simplicity, in

Table 2
Physical Conditions Considered in the Models

$n(\text{H})$ (cm^{-3})	r_{out} (pc)	A_v (mag)	T (K)	χ (Habing)	ζ (s^{-1})	Collapse ^a
Collapse Models						
2×10^4	0.3	13	10	1	1.3×10^{-17}	Long/short
2×10^5	0.3	120	10	1	1.3×10^{-17}	Long/short
2×10^6	0.3	1200	10	1	1.3×10^{-17}	Long/short
Proto-stellar Heating Models						
2×10^4	0.3	13	50	1	1.3×10^{-17}	Long/short
2×10^4	0.3	13	100	1	1.3×10^{-17}	Long/short
2×10^4	0.3	13	300	1	1.3×10^{-17}	Long/short
2×10^5	0.3	120	50	1	1.3×10^{-17}	Long/short
2×10^5	0.3	120	100	1	1.3×10^{-17}	Long/short
2×10^5	0.3	120	300	1	1.3×10^{-17}	Long/short
2×10^6	0.3	1200	50	1	1.3×10^{-17}	Long/short
2×10^6	0.3	1200	100	1	1.3×10^{-17}	Long/short
2×10^6	0.3	1200	300	1	1.3×10^{-17}	Long/short
UV Illumination Models						
2×10^4	0.03	3	50	1	1.3×10^{-17}	Long/short
2×10^4	0.03	3	50	10^2	1.3×10^{-17}	Long/short
2×10^4	0.03	3	50	10^4	1.3×10^{-17}	Long/short
2×10^4	0.03	3	100	1	1.3×10^{-17}	Long/short
2×10^4	0.03	3	100	10^2	1.3×10^{-17}	Long/short
2×10^4	0.03	3	100	10^4	1.3×10^{-17}	Long/short
2×10^4	0.15	7.5	50	1	1.3×10^{-17}	Long/short
2×10^4	0.15	7.5	50	10^2	1.3×10^{-17}	Long/short
2×10^4	0.15	7.5	50	10^4	1.3×10^{-17}	Long/short
2×10^4	0.15	7.5	100	1	1.3×10^{-17}	Long/short
2×10^4	0.15	7.5	100	10^2	1.3×10^{-17}	Long/short
2×10^4	0.15	7.5	100	10^4	1.3×10^{-17}	Long/short
2×10^4	0.3	13	50	1	1.3×10^{-17}	Long/short
2×10^4	0.3	13	50	10^2	1.3×10^{-17}	Long/short
2×10^4	0.3	13	50	10^4	1.3×10^{-17}	Long/short
2×10^4	0.3	13	100	1	1.3×10^{-17}	Long/short
2×10^4	0.3	13	100	10^2	1.3×10^{-17}	Long/short
2×10^4	0.3	13	100	10^4	1.3×10^{-17}	Long/short
Enhanced Cosmic-Rays Ionization Rate Models						
2×10^4	0.3	13	10	1	1.3×10^{-15}	Long/short
2×10^4	0.3	13	10	1	1.3×10^{-14}	Long/short
2×10^4	0.3	13	10	1	1.3×10^{-13}	Long/short
2×10^4	0.3	13	100	1	1.3×10^{-15}	Long/short
2×10^4	0.3	13	100	1	1.3×10^{-14}	Long/short
2×10^4	0.3	13	100	1	1.3×10^{-13}	Long/short
2×10^5	0.3	120	10	1	1.3×10^{-15}	Long/short
2×10^5	0.3	120	10	1	1.3×10^{-13}	Long/short
2×10^5	0.3	120	100	1	1.3×10^{-15}	Long/short
2×10^5	0.3	120	100	1	1.3×10^{-13}	Long/short

Note.

^a This refers to the length of the collapse: short-lived if Phase 1 is stopped when the final density is reached and long-lived if the collapse is some 10^5 yr longer after the final density is reached.

our models, we only consider the case of proto-stellar heating produced by a $15 M_{\odot}$ protostar.

The results of Phase 2 of our models are shown in Figure 2. For $T = 50$ K, the only P-bearing that is released

into the gas phase from the mantles is atomic P (at $\sim 3 \times 10^4$ yr). The PH_3 is not thermally desorbed at such low temperatures, and its solid abundance increases steadily during the warming-up phase thanks to hydrogenation (in particular, via $\# \text{PH}_2 + \# \text{H} \rightarrow \# \text{PH}_3$, where $\#$ denotes a grain mantle species). However, once the temperature reaches its maximum and is kept constant to $T = 50$ K, hydrogenation ceases because atomic P is thermally desorbed at this temperature (see above) and the PH_3 in the gas phase is slowly destroyed via proton transfer reactions with H_3^+ , HCO^+ , and H_3O^+ . In the gas phase, PO is formed via the reaction $\text{PH} + \text{O} \rightarrow \text{PO} + \text{H}$, while the formation of PN depends on the abundance of PO through $\text{N} + \text{PO} \rightarrow \text{PN} + \text{O}$. In fact, these two species reach an equilibrium at timescales of $\sim 3\text{--}4 \times 10^5$ yr for all densities showing similar abundances of a few 10^{-11} . In all models, PS remains very low and presents fractional abundances $\leq 10^{-12}$.

For $T = 100$ and 300 K, the evolution of the P-bearing species is similar, presenting a first jump in their abundances at $\sim 5 \times 10^4$ yr once the temperature of dust/gas reaches 100 K and all ices are thermally desorbed into the gas phase. Since PH_3 is the main reservoir of P in the mantles, this species is the most abundant for the first few 10^5 yr. After that, it gets destroyed via proton transfer reactions with mainly H_3O^+ . The decrease in the abundance of PH_3 is faster in models with $T = 300$ K because the destruction reaction $\text{PH}_3 + \text{H} \rightarrow \text{PH}_2 + \text{H}_2$ becomes efficient at higher temperatures due to its activation barrier of 735 K. Also, note that PH_3 is destroyed in the gas phase faster than other species such as PN and PO because, while PN/PO can re-form in the gas phase via reactions between P, PH, and PH_2 and O, O_2 , and N, the only gas-phase formation routes for PH_3 in our network are $\text{PH}_4^+ + \text{NH}_3 \rightarrow \text{PH}_3 + \text{NH}_4^+$ and $\text{PH}_4^+ + e^- \rightarrow \text{PH}_3 + \text{H}$ (see also Thorne et al. 1984).

For PO, this molecule tends to increase its abundance with time in most models and, except for densities $n(\text{H}) = 2 \times 10^6 \text{ cm}^{-3}$, PO always stays above PN. Once PS is desorbed from the mantles of dust grains, its abundance remains practically constant at $\sim 5\text{--}6 \times 10^{-12}$. In all these models, the abundance of P^+ remains below 10^{-13} .

The effects of the length of the collapse on the subsequent chemistry of P-bearing species during Phase 2 is illustrated in Figure 3. For warm temperatures ($T = 50$ K), the abundances in Phase 2 derived after considering a short-collapse phase are enhanced by at least a factor of 10 with respect to the long-collapse phase (see left panel in Figure 3). However, for higher temperatures, although the main P reservoir is PN instead of PH_3 at the beginning of Phase 2, the overall behavior of all P-bearing species is similar to that of the long-collapse scenario, since the gas-phase chemistry clearly dominates.

3.3. Effects of UV-photon Radiation

The effects of intense UV illumination on the chemistry of phosphorus are evaluated by varying the interstellar radiation field within ranges typical of photon-dominated regions (PDRs). We consider UV-photon radiation fields of $\chi = 100$ and 10^4 Habing; visual extinctions of $A_v = 3, 7.5,$ and 13 mag; and temperatures $T = 50$ and 100 K. These values are similar to those found in PDRs such as the Horsehead Nebula and the

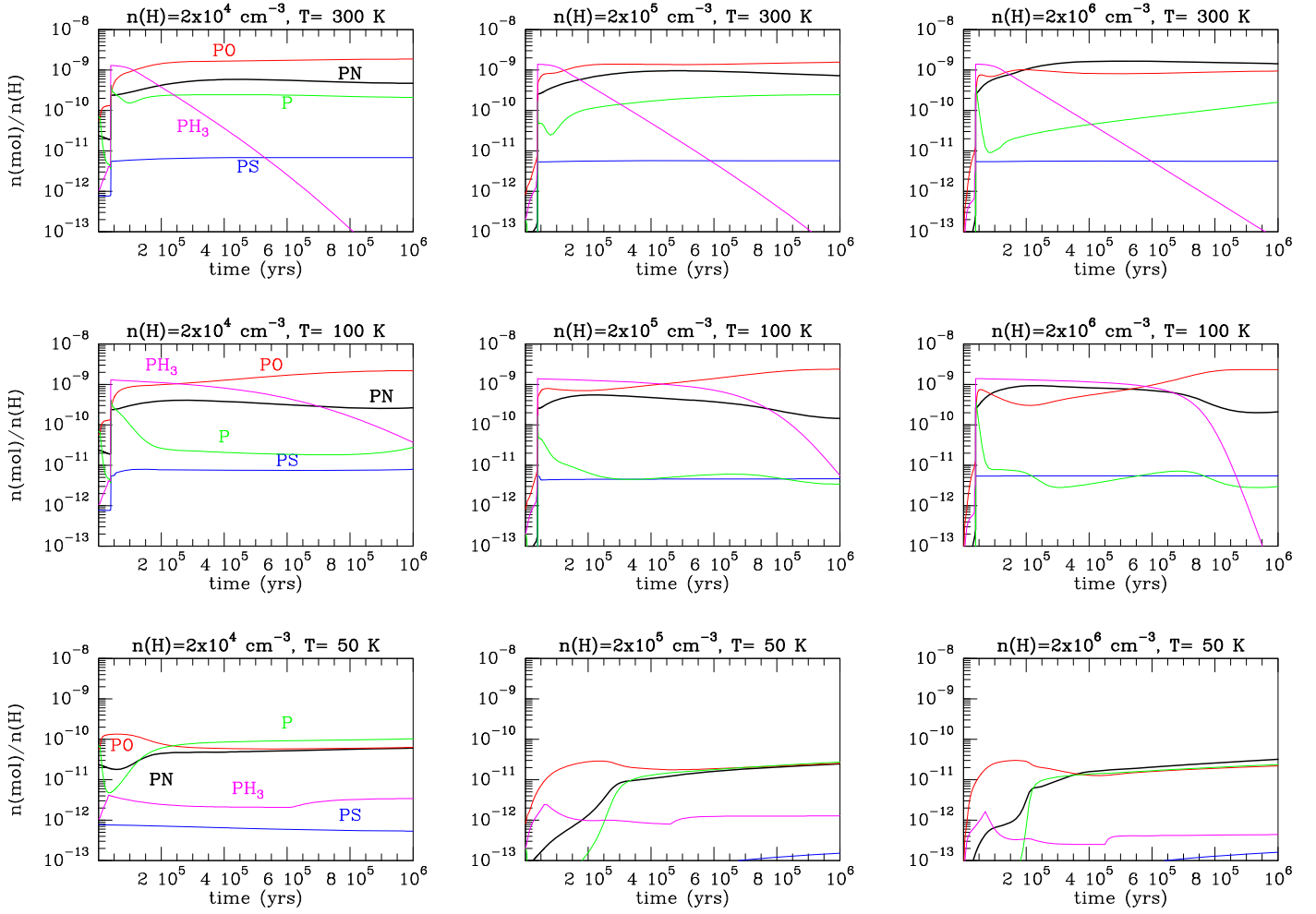


Figure 2. Abundances of P-bearing species as a function of time simulated during the warming up of the molecular envelope by a central protostar up to temperatures of 50 K (lower panels), 100 K (middle panels), and 300 K (upper panels). The final densities of the envelope are $n(H) = 2 \times 10^4$ (left), 2×10^5 (middle), and $2 \times 10^6 \text{ cm}^{-3}$ (right). These models have been run considering a long-lived collapse phase (Section 3.1).

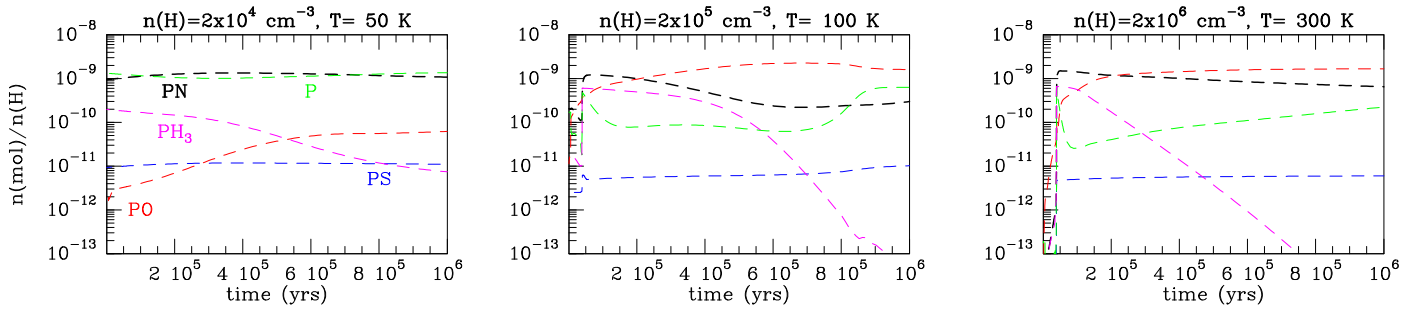


Figure 3. Examples of the evolution of the abundances of P-bearing species as a function of time simulated during the warming up of the molecular envelope by a central protostar considering a short-lived collapse phase. The abundances for models with $n(H) = 2 \times 10^4 \text{ cm}^{-3}$ and $T = 50 \text{ K}$ are at least a factor of 10 higher than those for the long-lived collapse case. For higher temperatures, however, the behavior of the P-bearing species is similar for both the short-lived and long-lived collapse scenarios.

Orion Bar (Schilke et al. 2001; Goicoechea et al. 2009). In the models, the temperature is kept constant, and the ices are instantaneously evaporated at the beginning of Phase 2. For completeness, we also present the results for models with $\chi = 1$ Habing (see Table 2). The results are reported in Figures 4 and 5.

From Figure 4, we find that at low extinctions ($A_V = 3 \text{ mag}$), PN and P are the most abundant P-bearing species (with

abundances $\geq 5 \times 10^{-10} - 10^{-9}$) for low- and intermediate-UV radiation fields ($\chi \leq 100$ Habing), while PO is efficiently destroyed. This is partly explained by the larger photodestruction rate of PO (with $\alpha = 3 \times 10^{-10} \text{ s}^{-1}$ and $\gamma = 2.0$, where the rate is calculated as $k = \alpha e^{-\gamma A_V}$) than of PN (with $\alpha = 5 \times 10^{-12} \text{ s}^{-1}$ and $\gamma = 3.0$). Note that these photodestruction rates have been estimated from the ones for NO and N_2 (see Harada

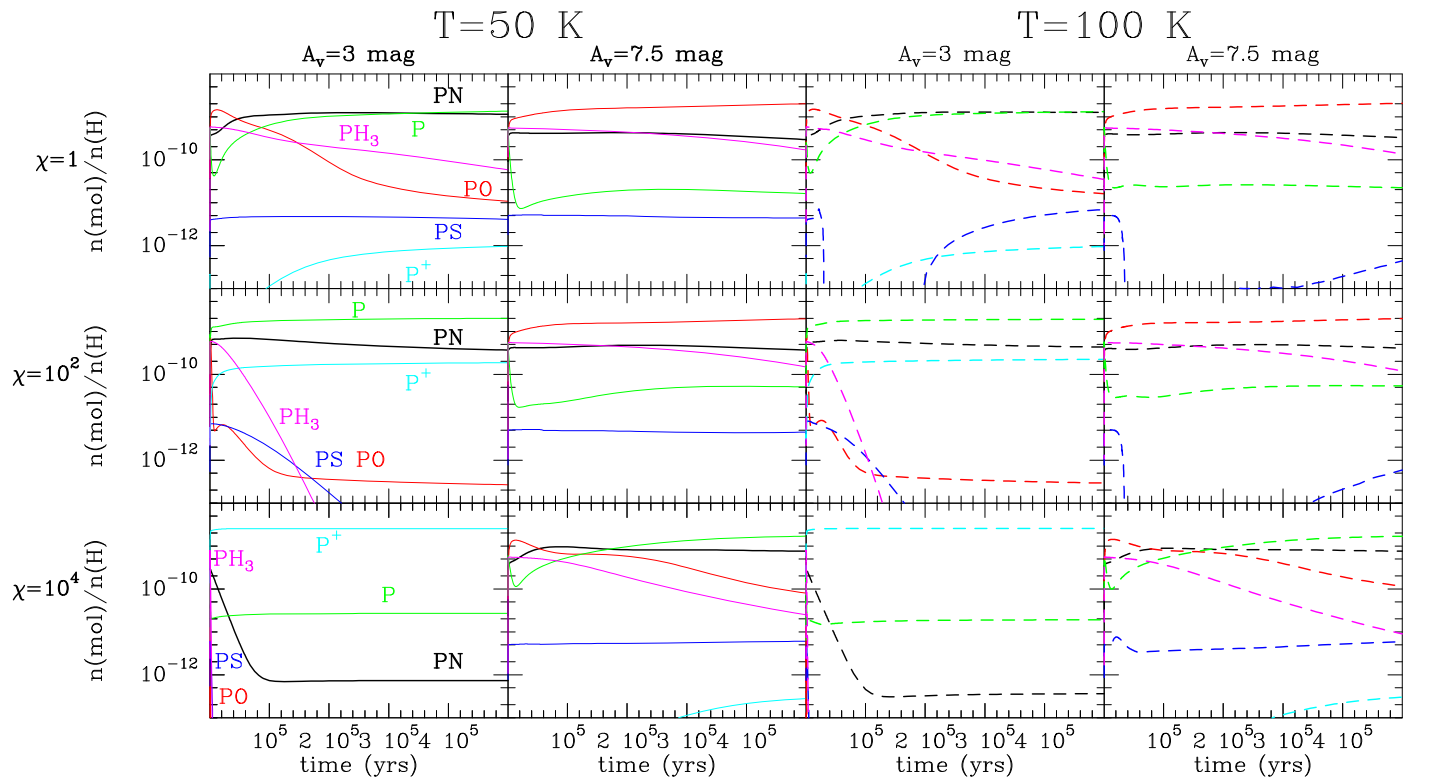


Figure 4. Evolution of P-bearing species under the effects of a radiation field of $\chi = 1, 100,$ and 10^4 Habing and for different visual extinctions ($A_v = 3$ and 7.5 mag) after a long-lived collapse. Solid lines denote models with $T = 50$ K, while the results from models with $T = 100$ K are shown with dashed lines. The results from models with $A_v = 13$ mag are identical to those obtained with $A_v = 7.5$ mag, and they are thus not shown.

et al. 2010) and, therefore, may be inaccurate. However, even in the case that PN were destroyed at higher rates via UV photodissociation, it would re-form again in the gas phase thanks to the large amounts of atomic N and P available in the gas phase, which react via $N + PO \rightarrow PN + O$ and $P + CN \rightarrow PN + C$, yielding PN. Like PO, PH_3 and PS are also increasingly photodissociated with increasing UV radiation field. Note that for even higher values of the UV field ($\chi = 10^4$ Habing), all molecular material is photodissociated, including PN, which shows abundances $\leq 10^{-12}$.

For higher extinctions ($A_v = 7.5$ mag), the behavior of all P-bearing species is similar to that obtained for the warming-up case with $T = 50$ and 100 K (see Figure 2), since UV photodissociation becomes practically ineffective at $A_v \geq 5$ mag. As expected, the results of models with $A_v = 13$ (not shown in Figure 4) are identical to those with $A_v = 7.5$ mag. The differences between models with $T = 50$ and 100 K are minimal except for PS, whose chemistry is more sensitive to higher temperatures (see dashed lines in Figure 4).

In models with a short-lived collapse phase (see Figure 5), PN is the most abundant P-bearing molecule with an abundance of $\sim 10^{-9}$, following P closely. As for the long-lived case, only small differences are found between models with $T = 50$ and 100 K. The results with $A_v = 7.5$ mag are also very similar to the short-lived warm-up models from Figure 3.

We finally note that in all UV-photon-illuminated models at low extinctions ($A_v = 3$ mag) or under high-UV radiation fields ($\chi = 10^4$ Habing), the abundance of PN always remains above that of PO.

3.4. Effects of Cosmic Rays

We now evaluate the effects of cosmic rays on the chemistry of P-bearing species. Cosmic rays are present in a variety of environments from shocks in molecular outflows (Podio et al. 2014), to star-forming regions (Ceccarelli et al. 2014; Fontani et al. 2017), to the GMCs in the Central Molecular Zone (CMZ) of our Galaxy (Goto et al. 2014). In Figures 6 and 7, we present the evolution of the P-bearing species within a molecular cloud with hydrogen volume densities $n(H) = 2 \times 10^4$ and $2 \times 10^5 \text{ cm}^{-3}$ and gas temperatures $T = 10$ and 100 K under the influence of cosmic rays whose ionization rates have been increased by factors of 100, 1000, and 10^4 (i.e., $\zeta = 1.3 \times 10^{-15}$, 1.3×10^{-14} , and $1.3 \times 10^{-13} \text{ s}^{-1}$, respectively). For the $T = 100$ K case, we consider that the ices are instantaneously evaporated at the beginning of Phase 2, as in Section 3.3. The physical conditions assumed for these models are presented in Table 2.

For the models with $n(H) = 2 \times 10^4 \text{ cm}^{-3}$ and $T = 10$ K, Figure 6 shows that a higher ζ (by factors of 100 and 1000) enhances the abundances of species such as PN and PO with respect to those predicted by the collapse models at the end of the collapse (see bottom left panel of Figure 1). This is due to (i) the nonthermal desorption of these species by cosmic-ray-induced secondary UV photons and (ii) the rapid photodissociation of PH_3 by this secondary UV field. As already noted in Section 3.2, once PH_3 is destroyed, it cannot re-form efficiently in the gas phase (Thorne et al. 1984), which unlocks high abundances of gas-phase P that can then be used to produce PN and PO.

For $\zeta = 1.3 \times 10^{-13} \text{ s}^{-1}$ (i.e., an enhancement in ζ by a factor of 10^4), molecules are rapidly photodissociated by the

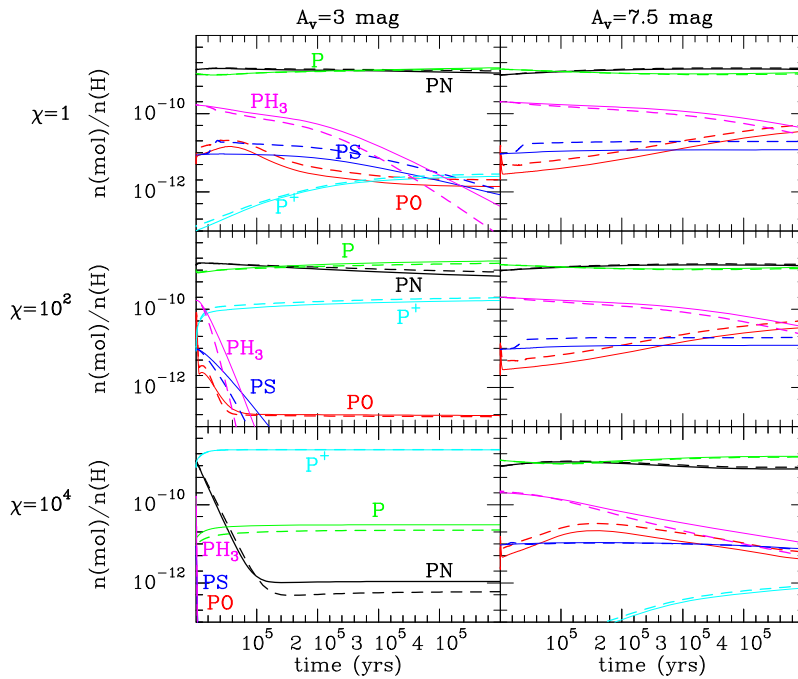


Figure 5. Same as Figure 4 but assuming a short-lived collapse phase. Solid lines indicate models with $T = 50 \text{ K}$, and dashed lines denote models with $T = 100 \text{ K}$. The abundance variations due to the change in temperature are minimal. The results from models with $A_v = 13 \text{ mag}$ are identical to those obtained with $A_v = 7.5 \text{ mag}$, and they are thus not shown.

strong secondary UV-photon radiation field, yielding large abundances of P⁺ and P. A similar trend is seen for higher temperatures ($T = 100 \text{ K}$), where PH₃ is rapidly destroyed in the gas phase in favor of PN and PO. In all models, PS is either destroyed or its abundance remains below $\leq 10^{-12}$. Here PN lies above PO with PO/PN ratios ~ 0.5 –1, except for the case with $T = 100 \text{ K}$ and $\zeta = 1.3 \times 10^{-13} \text{ s}^{-1}$, where PO is a factor of ~ 10 more abundant than PN.

For higher densities ($n(\text{H}) = 2 \times 10^5 \text{ cm}^{-3}$; see Figure 7), PN and PO are largely enhanced for $\zeta = 1.3 \times 10^{-13} \text{ s}^{-1}$ with respect to the low-density case thanks to the higher abundance of atomic N and O in these models, as they are more protected by the higher extinction. Atomic N and O yield higher abundances of PN and PO via reactions $\text{N} + \text{PO} \rightarrow \text{PN} + \text{O}$ and $\text{O} + \text{PH} \rightarrow \text{PO} + \text{H}$, respectively. Also, PN tends to be more abundant than PO in the high-density models.

We note that all models above consider a long-lived collapse phase (see Section 3.1). If the collapse phase is short-lived, the largest discrepancies are generally found for models with $\zeta \geq 1.3 \times 10^{-14} \text{ s}^{-1}$, where the PN and PO abundances decrease by factors of 10–100 with respect to the long-lived collapse case (see Figures 12 and 13). This is explained by the fact that in the short-lived collapse, the ice reservoir of P-bearing molecules is not as large as in the long-lived case, and the gas-phase P-bearing species are rapidly destroyed by the cosmic-ray-induced secondary UV photons.

3.5. Effects of C-type Shock Waves

3.5.1. General Behavior of P-bearing Species in C Shocks

Recently, P-bearing species such as PN and PO have been observed in shocked regions in molecular outflows (Yamaguchi et al. 2011; Lefloch et al. 2016). In addition, these species have also been detected in the turbulent GMCs in the central molecular zone (Rivilla et al. 2018), believed to be affected by widespread low-velocity shocks (Requena-Torres

et al. 2006) and likely under the influence of enhanced cosmic-ray ionization rates (Goto et al. 2014; Harada et al. 2015).

In Table 3, we present the physical parameters assumed for the C-type shock models used in our calculations. The pre-shock density is denoted by $n(\text{H})$, v_s is the shock speed, $T_{n,\text{max}}$ refers to the maximum temperature of the neutral fluid attained within the shock, and t_{sat} is the saturation time at which most of the material within the icy mantles of dust grains is sputtered into the gas phase (for more details, see Jiménez-Serra et al. 2008; Holdship et al. 2017). Different values of the cosmic-ray ionization rate ($\zeta = 10^{-17}$, 10^{-15} , and 10^{-13} s^{-1}) are also considered.

Figures 8 and 9 show the evolution of P-bearing molecules across the C-type shock structure for hydrogen gas densities of $n(\text{H}) = 2 \times 10^4$ and $2 \times 10^5 \text{ cm}^{-3}$, respectively. All species are enhanced early in the shock (at $\sim 60 \text{ yr}$ for $n(\text{H}) = 2 \times 10^4 \text{ cm}^{-3}$ and $\sim 6 \text{ yr}$ for $n(\text{H}) = 2 \times 10^5 \text{ cm}^{-3}$) due to sputtering. In particular, PH₃ and PN present enhancements larger than factors of 100 and 10, respectively. For models with shock speeds $v_s = 20 \text{ km s}^{-1}$, PH₃ stays relatively abundant throughout the shock after the sputtering of the ices (abundance between 10^{-10} and 10^{-9}), except in the presence of a high cosmic-ray ionization rate when PH₃ is more efficiently destroyed thanks to reactions with He⁺ and H₃⁺ (see model with $\zeta = 1.3 \times 10^{-13} \text{ s}^{-1}$ in Figure 8). For higher shock velocities ($v_s = 40 \text{ km s}^{-1}$), PH₃ is destroyed due to the endothermic reaction $\text{PH}_3 + \text{H} \rightarrow \text{PH}_2 + \text{H}_2$, whose activation energy is 735 K (see Table 1 in Charnley & Millar 1994). The destruction of PH₃ is even faster at higher temperatures (as in models with $n(\text{H}) = 2 \times 10^5 \text{ cm}^{-3}$ and $v_s = 40 \text{ km s}^{-1}$) or under the effects of cosmic rays.

From Figures 8 and 9, we find that PN remains relatively constant throughout the shock, with abundances typically falling between 1 and 5×10^{-10} . In contrast to PN, PO shows a different behavior depending on the model, becoming more abundant than PN in shocks with $n(\text{H}) = 2 \times 10^4 \text{ cm}^{-3}$ and $\zeta \geq 10^{-15} \text{ s}^{-1}$ or

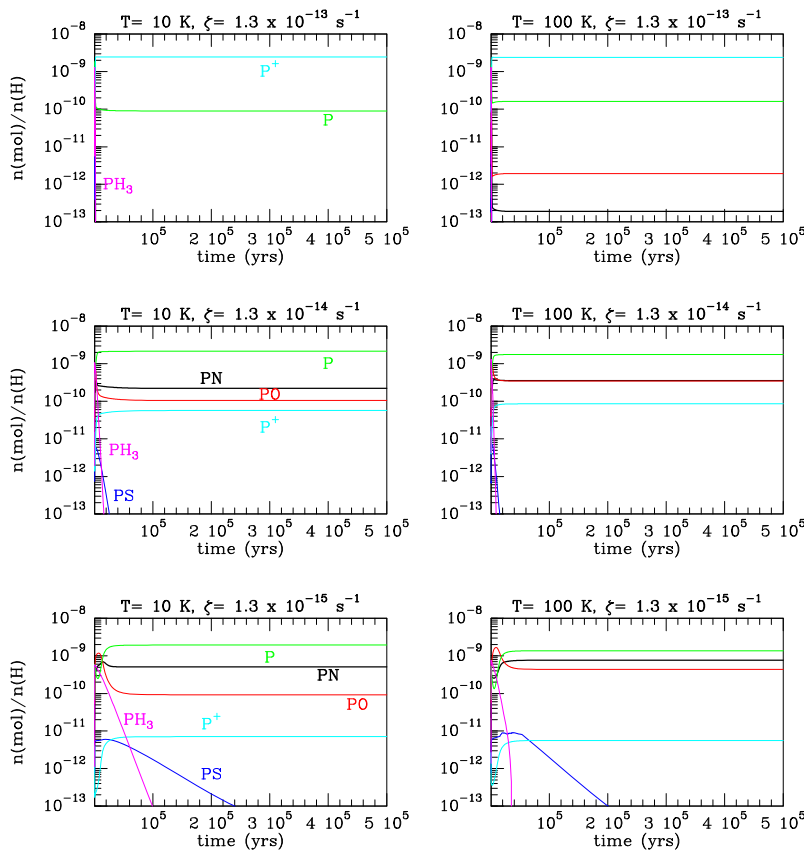


Figure 6. Evolution of the abundances of P-bearing species as a function of time simulated for a hydrogen density $n(\text{H}) = 2 \times 10^4 \text{ cm}^{-3}$; enhanced cosmic-ray ionization rates $\zeta = 1.3 \times 10^{-15}$, 1.3×10^{-14} , and $1.3 \times 10^{-13} \text{ s}^{-1}$; and gas temperatures $T = 10$ and 100 K , considering a long-lived phase for the collapse.

$n(\text{H}) = 2 \times 10^5 \text{ cm}^{-3}$ and $\zeta \geq 10^{-13} \text{ s}^{-1}$. After its injection into the gas phase by sputtering, PS experiences little change in the gas phase, except in models with $\zeta = 1.3 \times 10^{-13} \text{ s}^{-1}$, where it is destroyed by H_3^+ and He^+ .

For the short-lived collapse models, Figures 14 and 15 show that the most abundant P-bearing species within the shock are atomic P and PN, since they have not had enough time to deplete onto dust grains and subsequently hydrogenate during the collapse phase. Here PO becomes comparable in abundance to PN only for high cosmic-ray ionization rates ($\zeta \sim 10^{-13} \text{ s}^{-1}$).

3.5.2. Comparison with the Lefloch et al. (2016) Models

Lefloch et al. (2016) also presented models of the chemistry of P-bearing species in C-type shock waves using UCLCHEM and the C-shock parametric approximation of Jiménez-Serra et al. (2008). The chemical network used in these models, however, did not include either PH_3 or the endothermic reactions $\text{PH}_3 + \text{H} \rightarrow \text{PH}_2 + \text{H}_2$, $\text{PH}_2 + \text{H} \rightarrow \text{PH} + \text{H}_2$, and $\text{PH} + \text{H} \rightarrow \text{P} + \text{H}_2$ (with energy barriers ranging from 318 to 735 K; Charney & Millar 1994). This has important consequences for the evolution of the molecular abundances of PO and PN and its ratio in the shock, since, as opposed to the results of Lefloch et al. (2016), PN is always more abundant than PO in our models with standard values of the cosmic-ray ionization rate (i.e., $\zeta = 10^{-17} \text{ s}^{-1}$; see Figures 8 and 9). If the exothermic reactions of PH_3 , PH_2 , and PH with H are switched off in our models, we recover the results of Lefloch et al. (2016).

Millimeter observations of PN and PO in outflows (Lefloch et al. 2016) and Galactic center GMCs (Rivilla et al. 2018), however, indicate that the PO/PN abundance ratio is always

≥ 1 , which can be reconciled with our models only if (i) cosmic rays are significantly enhanced or (ii) the chemical network of PO is incomplete. In the following section (Section 4), we explore the possibility that the chemical network of PO lacks key formation reactions.

4. New Formation Reaction for PO

Codella et al. (2018) recently carried out the modeling of the chemistry of NO (a species with a molecular structure similar to that of PO) in hot corinos and shocked gas in molecular outflows. These authors noted that the enhancement of NO in the L1157-B1 shocked region is mainly produced by the reaction of atomic nitrogen, N, with OH. The equivalent reaction for P ($\text{P} + \text{OH} \rightarrow \text{PO} + \text{H}$), however, does not exist in any database, and, given the similarity between NO and PO, the reaction between P and OH may also be efficient (note that the activation barrier is only $\sim 15 \text{ K}$; see Table 4).

We have therefore rerun all our models after including the reaction $\text{P} + \text{OH} \rightarrow \text{PO} + \text{H}$ in our chemical network. As a reaction rate, we have assumed the one from the analogous reaction with NO (see Table 4). Our results show that for most models, the inclusion of this reaction does not appreciably affect the final abundance of PO, since it is enhanced only by factors of ~ 2 – 3 . However, for models with C-type shock waves, the abundance of PO can be enhanced by several orders of magnitude (see Figure 10). From this figure, it is clear that thanks to the new reaction $\text{P} + \text{OH} \rightarrow \text{PO} + \text{H}$, PO becomes even more abundant than PN within the shock for standard cosmic-ray ionization rates, in contrast to our results from

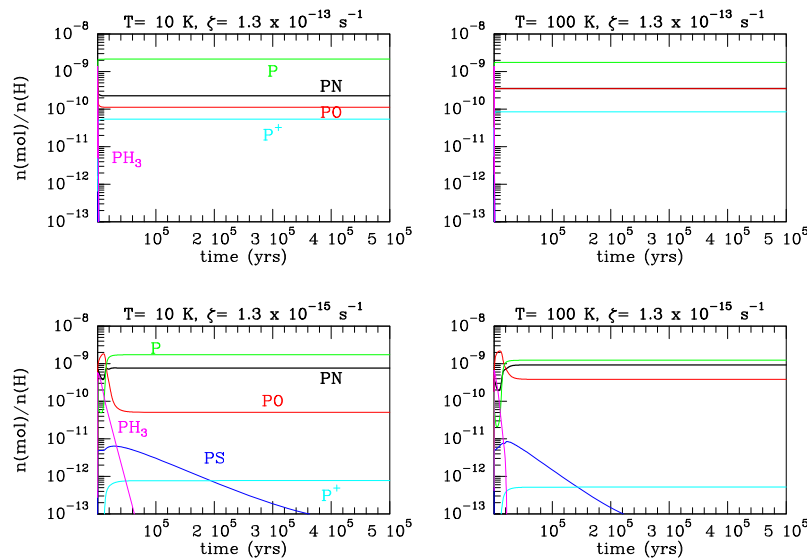


Figure 7. Evolution of the abundances of P-bearing species as a function of time simulated for a hydrogen density $n(\text{H}) = 2 \times 10^5 \text{ cm}^{-3}$, enhanced cosmic-ray ionization rates $\zeta = 1.3 \times 10^{-15}$ and $1.3 \times 10^{-13} \text{ s}^{-1}$, and gas temperatures $T = 10$ and 100 K , considering a long-lived phase for the collapse.

Table 3
Physical Parameters Assumed for the C-type Shock Models

$n(\text{H})$ (cm^{-3})	v_s (km s^{-1})	$T_{n,\text{max}}$ (K)	t_{sat} (yr)	ζ (s^{-1})	Collapse ^a
2×10^4	20	900	57.0	1.3×10^{-17}	Long/short
2×10^4	20	900	57.0	1.3×10^{-15}	Long/short
2×10^4	20	900	57.0	1.3×10^{-13}	Long/short
2×10^4	40	2200	45.5	1.3×10^{-17}	Long/short
2×10^4	40	2200	45.5	1.3×10^{-15}	Long/short
2×10^4	40	2200	45.5	1.3×10^{-13}	Long/short
2×10^5	20	800	5.7	1.3×10^{-17}	Long/short
2×10^5	20	800	5.7	1.3×10^{-15}	Long/short
2×10^5	20	800	5.7	1.3×10^{-13}	Long/short
2×10^5	40	4000	4.6	1.3×10^{-17}	Long/short
2×10^5	40	4000	4.6	1.3×10^{-15}	Long/short
2×10^5	40	4000	4.6	1.3×10^{-13}	Long/short

Notes. All models assume $\chi = 1$ Habing.

^a This refers to the length of the collapse during Phase 1 in our modeling (see also the notes in Table 2).

Section 3.5. This occurs thanks to the high temperatures (of thousands of K) attained within the shock. In fact, if this reaction were as efficient as proposed here, the PO/PN ratio in shocks would be dominated by this reaction and not by enhanced cosmic rays any longer (see lower panels of Figure 10). Theoretical calculations and/or experiments are needed to clearly establish the efficiency of the PO gas-phase formation route $\text{P} + \text{OH} \rightarrow \text{PO} + \text{H}$.

5. Comparison with Observations

5.1. PN and PO

In this section, we compare our modeling results to the abundances of PN and PO measured toward low-mass/high-mass starless/pre-stellar cores (Turner et al. 1990; Mininni et al. 2018), massive hot cores (Turner et al. 1990; Rivilla

et al. 2016), GMCs in the Galactic center (Rivilla et al. 2018), and molecular outflows (Yamaguchi et al. 2011; Lefloch et al. 2016).

1. *Cold cloud and starless/pre-stellar cores.*—Early millimeter observations of PN toward a sample of low-mass cold cloud cores (with $T \sim 10 \text{ K}$) provided upper limits to the abundance of PN of $\leq 0.2\text{--}4 \times 10^{-11}$ in cold cloud cores (Turner et al. 1990). Recent higher-sensitivity observations performed toward the L1544 pre-stellar core reveal that PN remains undetected with upper limits of $\leq 4.6 \times 10^{-13}$ (as derived from the data set of Jiménez-Serra et al. 2016). As shown in Figure 1 for the long-lived collapse case (see bottom panels), these upper limits are consistent with the low gas-phase PN abundances predicted at a few 10^5 yr after the end of the collapse in cold high-density cores (with hydrogen gas densities $\geq 2 \times 10^5 \text{ cm}^{-3}$). For massive starless cores, which show slightly warmer temperatures (with $T \sim 25\text{--}30 \text{ K}$; Fontani et al. 2016), the derived abundances of PN are $\sim 10^{-11}$ and 5×10^{-12} (Mininni et al. 2018), in agreement with those predicted by our models under warm temperatures for $n(\text{H}) \geq 2 \times 10^5 \text{ cm}^{-3}$ and timescales of a few 10^5 yr (see models with $T = 50 \text{ K}$ in Figure 2). No upper limits are available for PO toward low-mass/high-mass cold cores.
2. *Massive hot cores.*—The derived abundance of PN in hot molecular cores typically ranges from some 10^{-12} to almost 10^{-9} (Turner et al. 1990; Rivilla et al. 2016). The gas temperatures and hydrogen gas densities derived for these regions are $\sim 30\text{--}150 \text{ K}$ and $\sim 10^5\text{--}10^6 \text{ cm}^{-3}$, respectively (see, e.g., Turner et al. 1990). The PN abundances predicted for timescales $\leq 2\text{--}3 \times 10^5 \text{ yr}$ (typical of hot cores) by models with $T \sim 50\text{--}100 \text{ K}$ and $n(\text{H}) \sim 2 \times 10^5\text{--}2 \times 10^6 \text{ cm}^{-3}$ provide similar PN abundances to those observed (see upper and middle panels in Figure 2). The PO abundances obtained in our models ($\sim 0.3\text{--}6.0 \times 10^{-10}$) also well reproduce those observed in hot molecular cores (Rivilla et al. 2016).

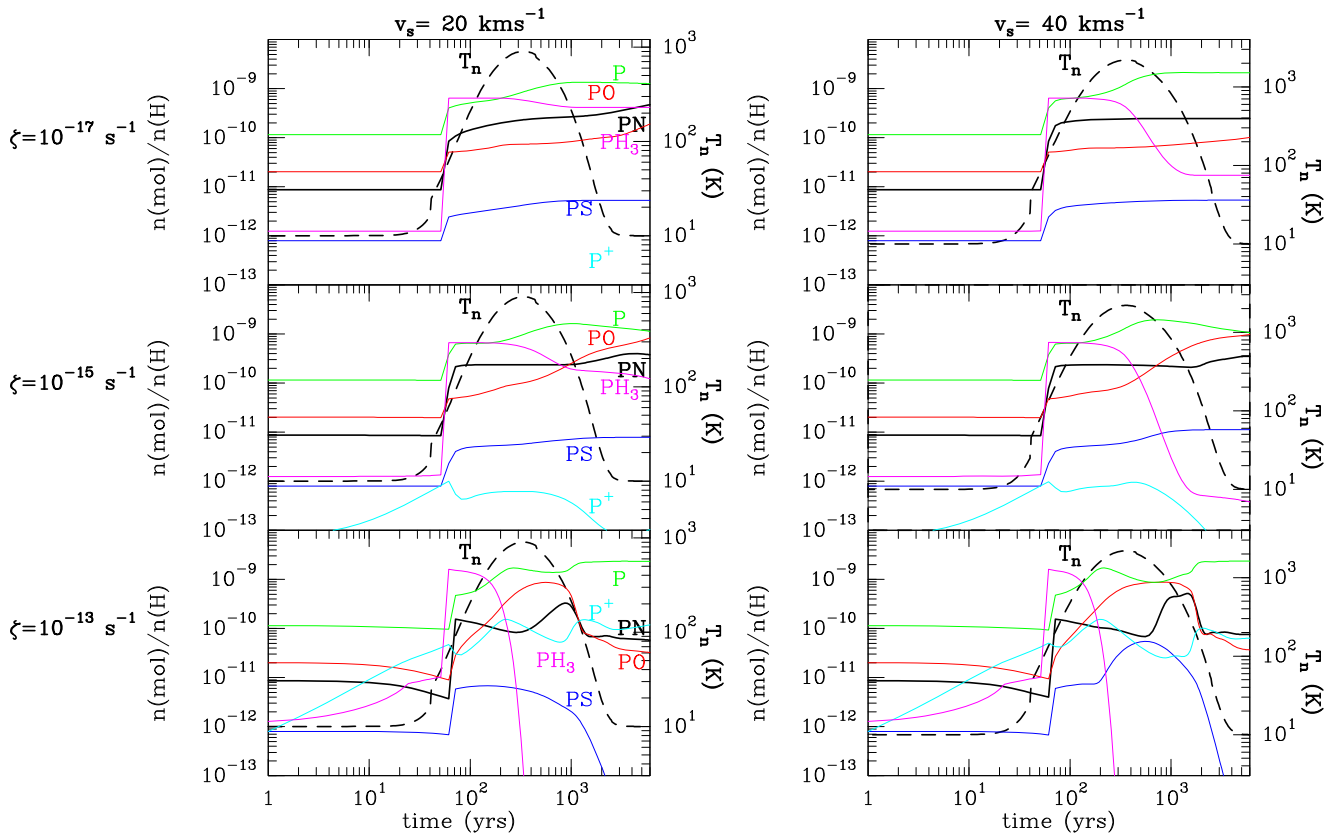


Figure 8. Evolution of the abundances of P-bearing species as a function of time across two C-type shocks with a pre-shock density of $n(\text{H}) = 2 \times 10^4 \text{ cm}^{-3}$ and shock speeds of $v_s = 20$ (left panels) and 40 (right panels) km s^{-1} . Dashed lines indicate the evolution of the temperature of the neutral fluid within the shock (T_n). To simulate the extreme conditions in the Galactic center, we also consider that the shocked gas is affected by enhanced cosmic-ray ionization rates of $\zeta = 10^{-15}$ and 10^{-13} s^{-1} . These models have been obtained considering a long-lived collapse.

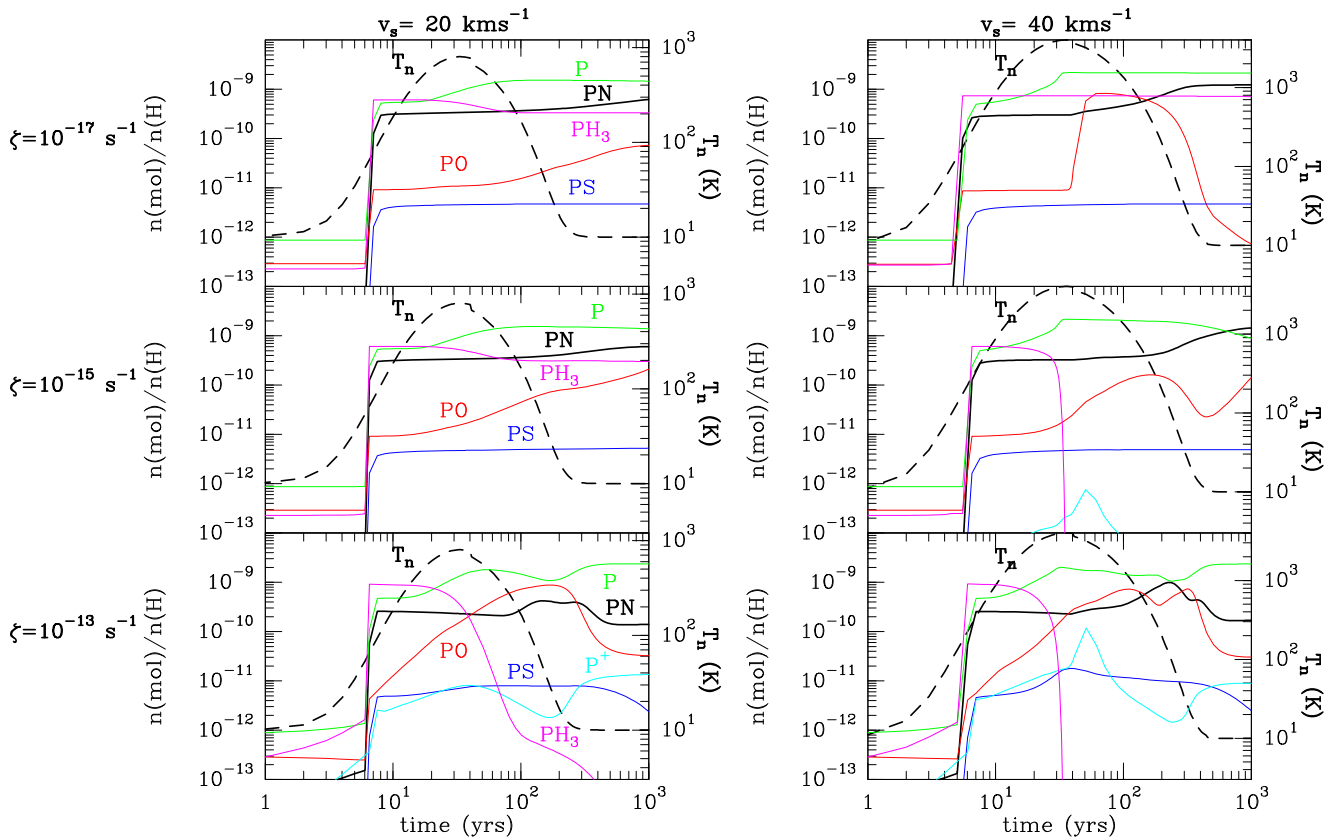


Figure 9. Same as Figure 9 but for a pre-shock density of $n(\text{H}) = 2 \times 10^5 \text{ cm}^{-3}$.

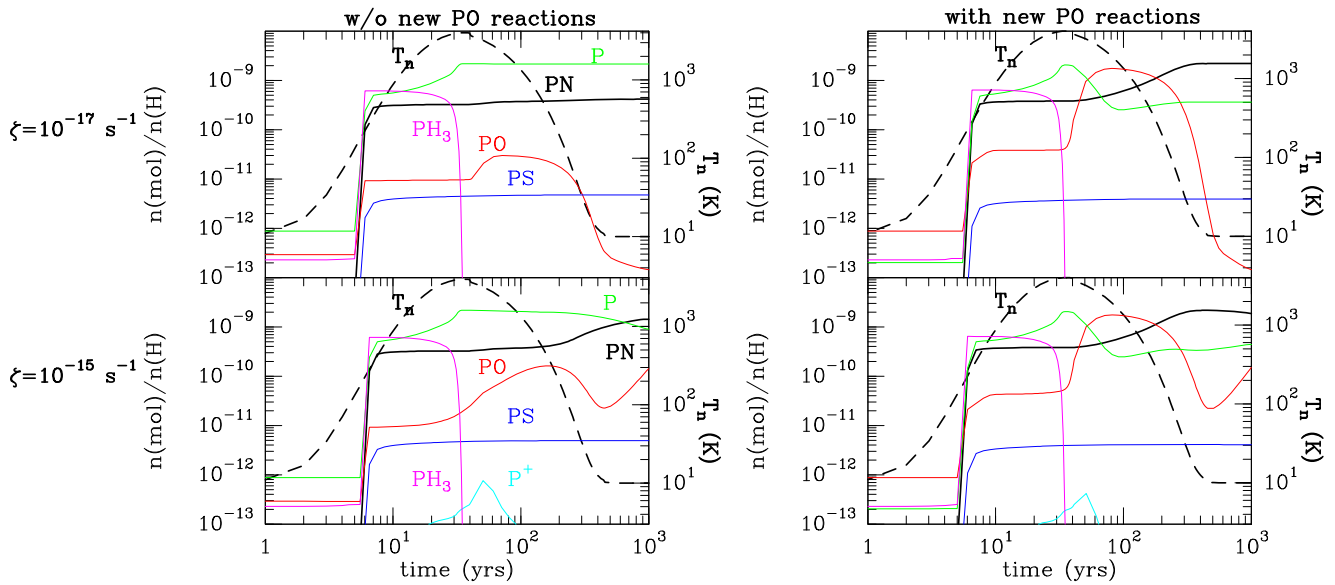


Figure 10. Comparison of models obtained for $n(\text{H}) = 2 \times 10^5 \text{ cm}^{-3}$ and $v_s = 40 \text{ km s}^{-1}$ using the original chemical network (as presented in Section 2; left panels) and a new network where the proposed PO formation route $\text{P} + \text{OH} \rightarrow \text{PO} + \text{H}$ is included. Models with cosmic-ray ionization rates of $\zeta \sim 10^{-17}$ (upper panels) and 10^{-15} (lower panels) s^{-1} are presented. All models shown here consider a long-lived collapse phase.

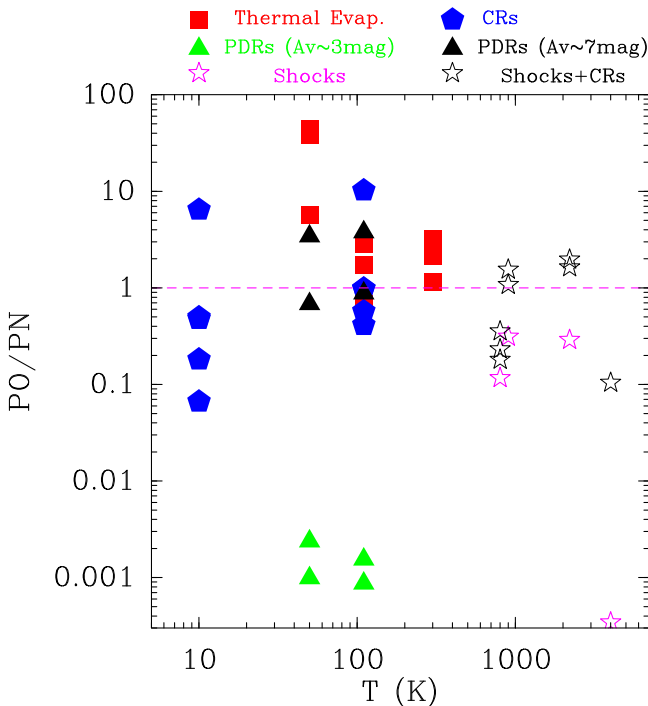


Figure 11. Compilation of the PO/PN abundance ratios obtained within our models as a function of temperature. The ratios corresponding to two different timescales are shown for every model: 10^5 yr for models considering protostellar heating (red squares), cosmic rays (blue pentagons), and UV radiation (green and black triangles) and 10^3 yr for models with shocks and shocks + cosmic rays (magenta and black stars). The dashed magenta line denotes the PO/PN ratio of 1.

3. *Galactic center GMCs.*—Rivilla et al. (2018) recently carried out observations of PN and PO toward a sample of quiescent GMCs in the Galactic center that present either shock-dominated or radiation-dominated chemistries. Rivilla et al. (2018) found a positive

Table 4

Reaction Rate Assumed for the Models of Section 4, as Extracted from UMIST

Reaction	α ($\text{cm}^3 \text{ s}^{-1}$)	β	γ (K)
$\text{P} + \text{OH} \rightarrow \text{PO} + \text{H}$	6.1×10^{-11}	-0.23	14.9

trend between the abundances of PN and ^{29}SiO , which suggests that PN may be formed in shocks as SiO. The derived PN abundances toward shock-dominated quiescent GMCs are $\sim 0.5\text{--}5 \times 10^{-11}$ (Rivilla et al. 2018), i.e., within a factor of 10 of those predicted by our models with $v_s = 20 \text{ km s}^{-1}$, $n(\text{H}) = 2 \times 10^4 \text{ cm}^{-3}$, and high cosmic-ray ionization rates (see Figure 8, left panels). The measured PO/PN ratio of 1.5 in the quiescent GMC G+0.693-0.03 also supports the models with enhanced cosmic rays, although, as discussed in Section 4, a PO/PN ratio ≥ 1 could also be obtained in shocks if the reaction $\text{P} + \text{OH} \rightarrow \text{PO} + \text{H}$ were efficient. This reaction is currently not included in any chemical database. For the quiescent GMCs affected by radiation, only upper limits to the abundance of PN are available. This is consistent with our results of the chemistry of P-bearing species in PDRs, for which UV radiation fields $\chi \sim 10^4$ Habing destroy PN and PO down to abundances $\leq 10^{-12}$ (for $A_v = 3 \text{ mag}$; see Figures 4 and 5). The lack of detection of PN in the Orion Bar (Cuadrado et al. 2015; Rivilla et al. 2018) confirms this hypothesis (the Orion Bar is affected by a UV radiation field of $\chi = 5 \times 10^4$ Habing; see, e.g., Schilke et al. 2001).

4. *Molecular outflows.*—In Lefloch et al. (2016), the preferred model to explain the PO/PN abundance ratio of ~ 2 measured in the L1157-B1 shock cavity involves a shock with gas densities of 10^5 cm^{-3} , shock speeds of 40 km s^{-1} , and a standard cosmic-ray ionization rate

($1.5 \times 10^{-17} \text{ s}^{-1}$). Unless the chemical network of PO is incomplete (see Section 4), our shock model results suggest that the chemistry of P-bearing species in L1157-B1 is likely affected by cosmic rays. This is consistent with the detection of molecular ions such as HOCO^+ and SO^+ in L1157-B1, which requires a cosmic-ray ionization rate of $\sim 3 \times 10^{-16} \text{ s}^{-1}$ (Podio et al. 2014). Theoretical studies and/or new experiments are needed to establish whether the reaction $\text{P} + \text{OH} \rightarrow \text{PO} + \text{H}$ is indeed as efficient as proposed in Table 4.

5.2. Phosphine (PH_3)

Although phosphine (PH_3) has been detected in the atmospheres of Jupiter and Saturn (Larson et al. 1977; Weisstein & Serabyn 1994), there is no evidence of its presence in star-forming regions. According to our models in Section 3, PH_3 tends to be destroyed rapidly in the gas phase (for timescales shorter than a few 10^4 yr) after its ejection from dust grains, as also noted by Charnley & Millar (1994). Nevertheless, for some cases, PH_3 could remain in the gas phase for longer timescales in hot molecular cores and shocked regions, reaching gas-phase abundances as high as $\sim 10^{-9}$ (see Figures 2, 8, and 9). Then, PH_3 could be observed via its $J = 1 \rightarrow 0$ and $J = 2 \rightarrow 1$ rotational transitions at 266.9 and 533.8 GHz, respectively, with instruments such as the IRAM 30 m telescope, ALMA, and SOFIA. To our knowledge, no observations (or reported upper limits) exist for this molecule toward hot molecular cores. However, upper limits to the abundance of PH_3 have been reported toward the B1 shocked region in the L1157 molecular outflow (of $\leq 10^{-9}$; Lefloch et al. 2016). These upper limits, which were inferred from high-sensitivity IRAM 30 m telescope data,⁶ are consistent with the abundances predicted by our models considering the interaction of shock waves (Figures 8 and 9).

6. The PO/PN Ratio

For the sources where PO has been detected in the ISM (e.g., hot cores, molecular outflows, and the quiescent Galactic center GMC G+0.693; see Lefloch et al. 2016; Rivilla et al. 2016, 2018), observations have revealed that the PO/PN ratio is always ≥ 1 . Our models in Section 3 have, however, shown that the PO/PN ratio may become ≤ 1 for certain physical conditions and energetic phenomena.

Figure 11 presents the PO/PN ratios obtained by our models for timescales of 10^5 yr (typical of hot molecular cores and Galactic center GMCs; Requena-Torres et al. 2006; Rivilla et al. 2016) for the models of proto-stellar heating, cosmic rays, and UV radiation and 10^3 yr (typical of outflows; see, e.g., Podio et al. 2014) for the models with shocks and shocks with cosmic rays. All models consider a long-lived collapse phase. As seen from Figure 11, the different energetic processes tend to cluster the PO/PN ratios toward different parts of the diagram. While proto-stellar heating and cosmic rays typically give $\text{PO/PN} \geq 1$, this ratio is expected to be $\ll 1$ in PDRs (with $A_v \sim 3 \text{ mag}$). This explains why the observed PO/PN ratios in hot molecular cores are ≥ 1 (Rivilla et al. 2016). For PDRs with higher extinction (with $A_v \sim 7 \text{ mag}$), the

⁶ They belong to the ASAI Large Program (Astrochemical Surveys at IRAM), and the upper limits of the PH_3 abundance were estimated using an rms noise level of 3 mK over a line width of 5 km s^{-1} .

chemistry of P-bearing species behaves in a similar way to that affected by proto-stellar heating, since the efficiency of molecular photodissociation drastically decreases at extinctions $A_v \geq 5 \text{ mag}$.

For models with shocks, the PO/PN ratio is ≤ 1 in the absence of cosmic rays, while this ratio is boosted above 1 under their effects. However, note that this trend may be a result of the incompleteness of the PO chemical network (see Section 4). If the PO formation reaction proposed in Table 4 is experimentally or theoretically confirmed, the PO/PN ratios in shocks are also expected to be ≥ 1 .

Finally, for models with a short-lived collapse phase, the derived PO/PN ratios typically fall below 1, except for a few exceptions that involve enhancements of the cosmic-ray ionization rate by factors of 10^2 and 10^4 .

7. Conclusions

Such P-bearing species as PN and PO have started to be routinely detected in regions of the ISM affected by different energetic phenomena, such as proto-stellar heating, cosmic rays, UV radiation, and shock waves. In this paper, we have revisited the chemistry of phosphorus in the ISM under energetic processing, putting special emphasis on the predicted ratio between PN and PO.

Our models show that a long-lived collapse is required to reproduce the PO/PN ratios ≥ 1 observed in hot molecular cores (see Section 6). The models considering UV illumination confirm that P-bearing species are expected to be destroyed under the effects of strong UV radiation fields, as observed in the Orion Bar and Galactic center GMCs (Section 3.3). Moderate UV radiation fields ($\chi \sim 100 \text{ Habing}$), however, should yield detectable abundances of P-bearing species such as PN, PO, and PS. Models with enhanced cosmic-ray ionization rates provide a wide range of PO/PN ratios, although PN tends to be more abundant than PO. For models with C-type shock waves, an observed ratio $\text{PO/PN} \geq 1$ is only obtained under the effects of enhanced rates of cosmic rays, unless the chemical network of PO is incomplete (Section 4). We propose that the reaction $\text{P} + \text{OH} \rightarrow \text{PO} + \text{H}$ (currently missing in all chemical databases) could be as efficient as its analog reaction involving NO. Theoretical/experimental investigations are needed to establish the actual efficiency of this gas-phase formation route of PO.

We are thankful for the constructive comments from the referee, which helped to improve the original version of the manuscript. IJ-S and DQ acknowledge the financial support received from the STFC through an Ernest Rutherford Fellowship and Grant (proposal numbers ST/L004801 and ST/M004139). JH and SV acknowledge support from the STFC (grant number ST/M001334/1).

Appendix Additional Figures

In this section, we present the figures for those models that consider a short-lived collapse phase and enhanced cosmic-ray ionization rates (Figures 12 and 13) and shocks (Figures 14 and 15).

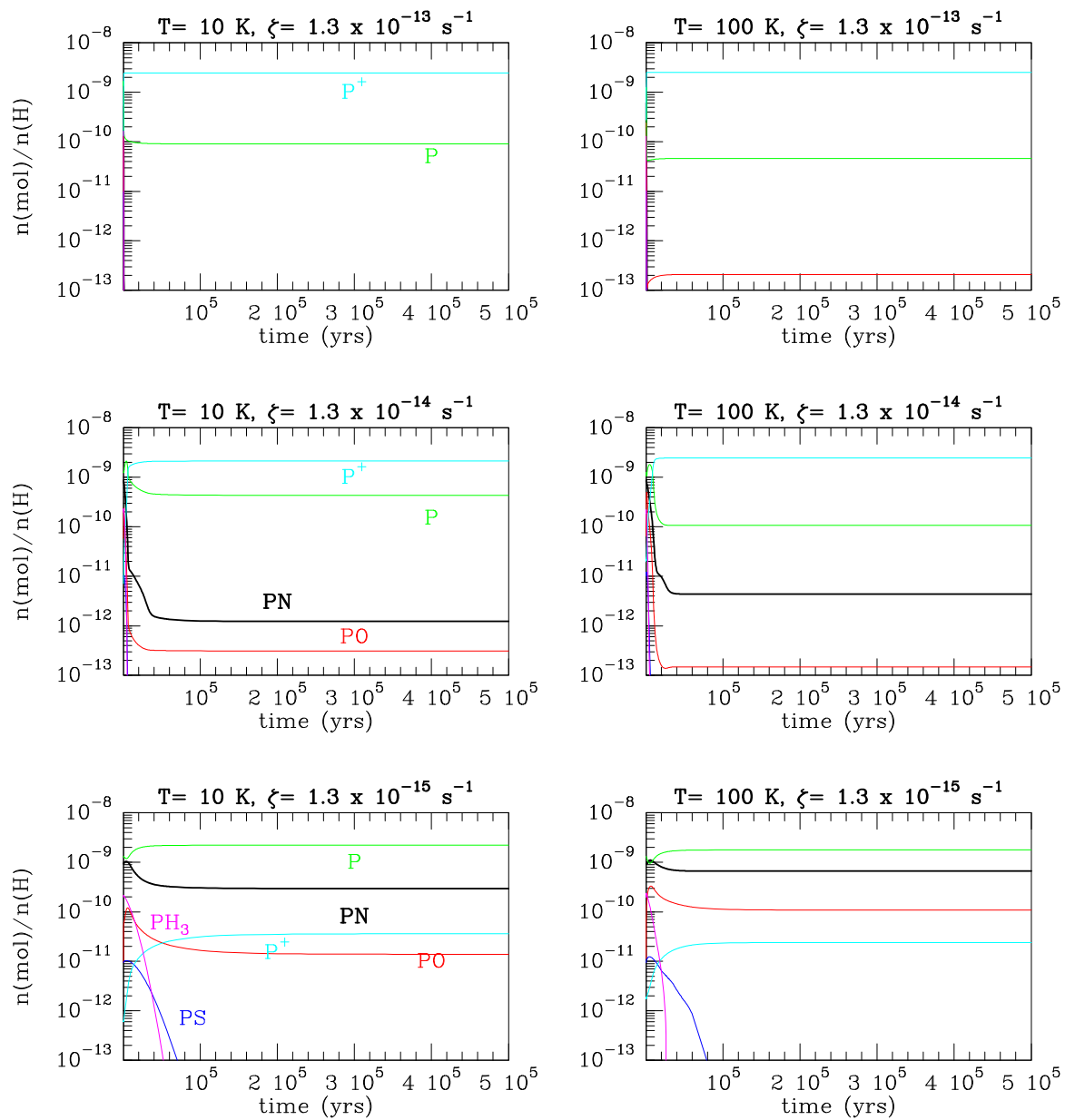


Figure 12. Evolution of the abundances of P-bearing species as a function of time simulated for a hydrogen density $n(\text{H}) = 2 \times 10^4 \text{ cm}^{-3}$, enhanced cosmic-ray ionization rates $\zeta = 1.3 \times 10^{-15}$ and $1.3 \times 10^{-13} \text{ s}^{-1}$, and gas temperatures $T = 10$ and 100 K , considering a short-lived phase for the collapse.

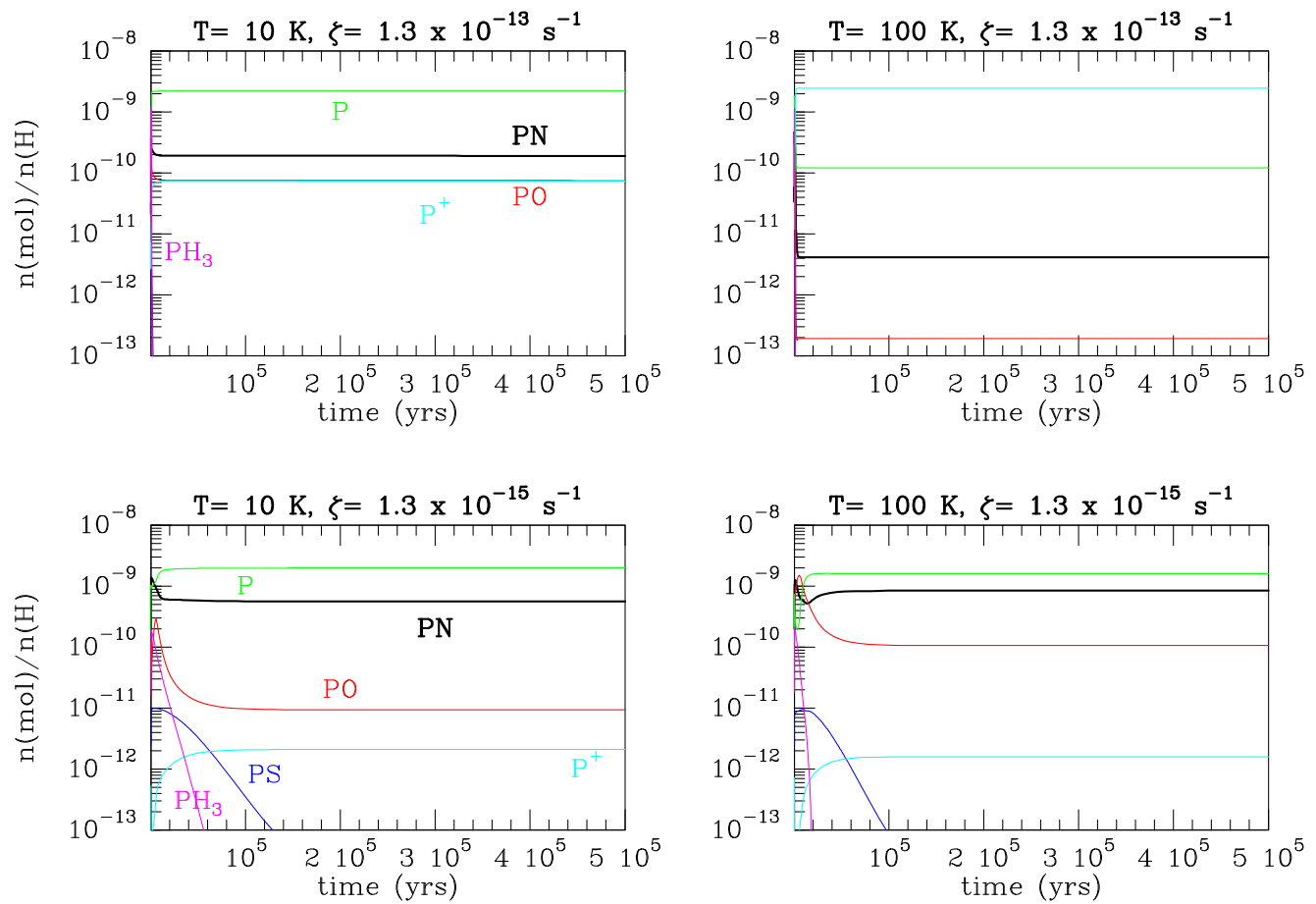


Figure 13. Evolution of the abundances of P-bearing species as a function of time simulated for a hydrogen density $n(\text{H}) = 10^5 \text{ cm}^{-3}$, enhanced cosmic-ray ionization rates $\zeta = 1.3 \times 10^{-15}$ and $1.3 \times 10^{-13} \text{ s}^{-1}$, and gas temperatures $T = 10$ and 100 K , considering a short-lived phase for the collapse.

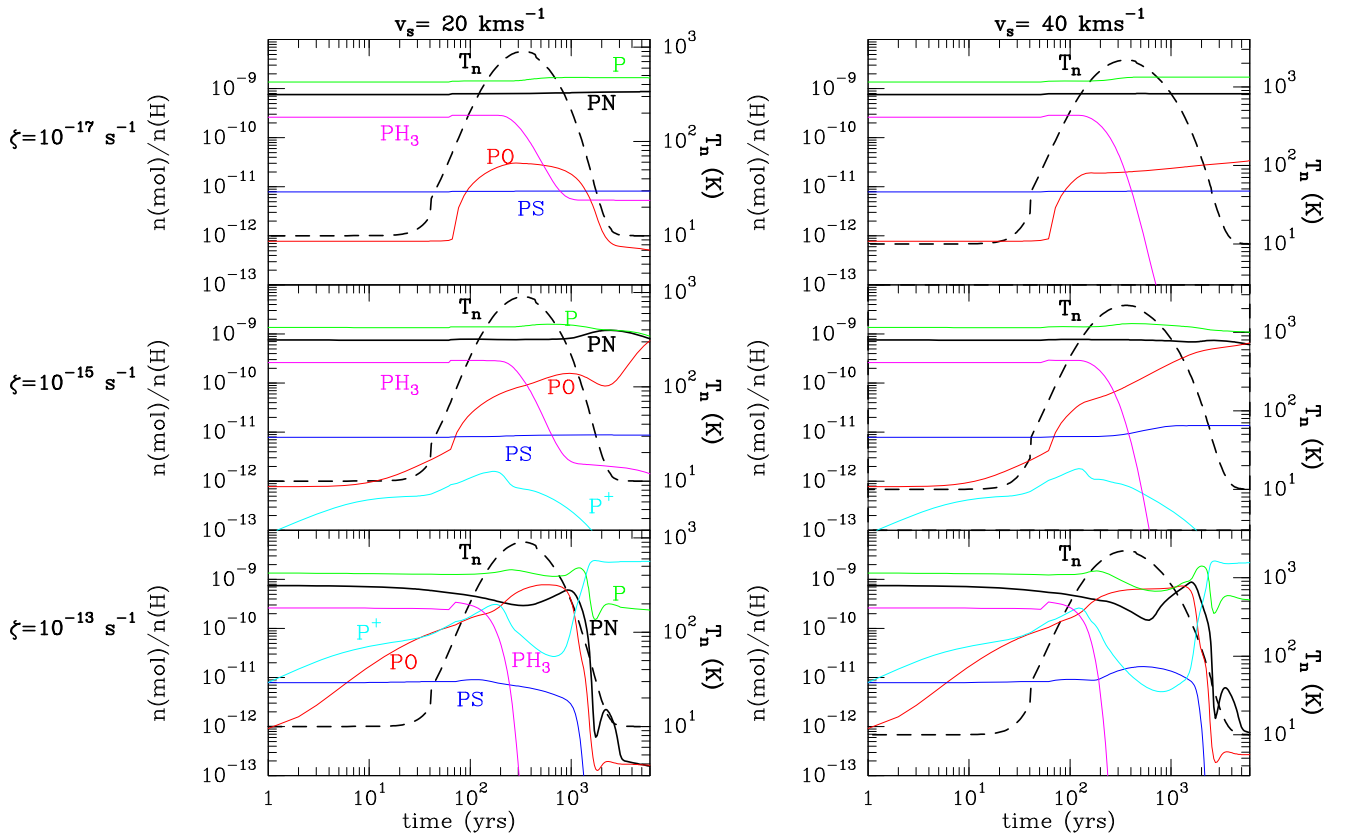


Figure 14. Evolution of the abundances of P-bearing species as a function of time simulated for a hydrogen density $n(\text{H}) = 10^4 \text{ cm}^{-3}$, shock velocities $v_s = 20$ and 40 km s^{-1} , and cosmic-ray ionization rates $\zeta = 1.3 \times 10^{-17}$, 1.3×10^{-15} , and $1.3 \times 10^{-13} \text{ s}^{-1}$. These models consider a short-lived phase for the collapse.

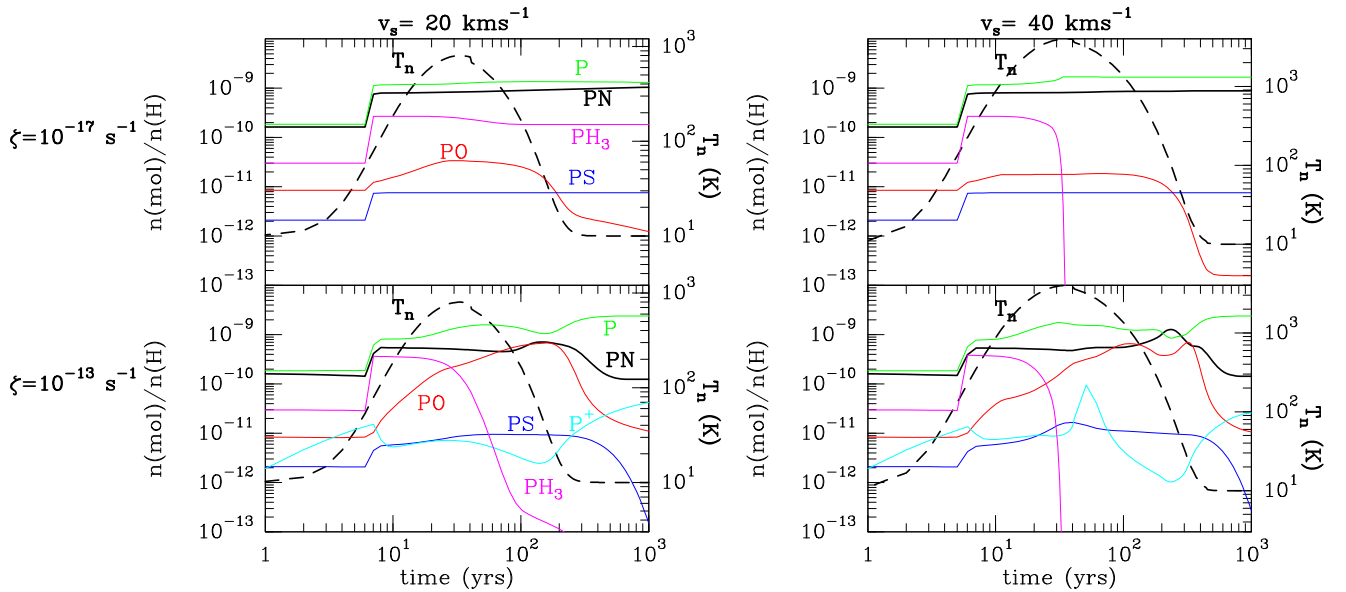


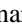



Figure 15. Evolution of the abundances of P-bearing species as a function of time simulated for a hydrogen density $n(\text{H}) = 2 \times 10^5 \text{ cm}^{-3}$, shock velocities $v_s = 20$ and 40 km s^{-1} , and cosmic-ray ionization rates $\zeta = 1.3 \times 10^{-17}$ and $1.3 \times 10^{-13} \text{ s}^{-1}$. These models consider a short-lived phase for the collapse.

ORCID iDs

Izaskun Jiménez-Serra  <https://orcid.org/0000-0003-4493-8714>
 Serena Viti  <https://orcid.org/0000-0001-8504-8844>
 David Quénard  <https://orcid.org/0000-0002-2969-3985>
 Jonathan Holdship  <https://orcid.org/0000-0003-4025-1552>

References

- Agúndez, M., Cernicharo, J., Decin, L., Encrenaz, P., & Teyssier, D. 2014a, *ApJL*, **790**, L27A
- Agúndez, M., Cernicharo, J., & Guélin, M. 2007, *ApJL*, **662**, L91A
- Agúndez, M., Cernicharo, J., & Guélin, M. 2014b, *A&A*, **570A**, 45A
- Agúndez, M., Cernicharo, J., Pardo, J. R., Guélin, M., & Phillips, T. G. 2008, *A&A*, **485L**, 33A
- Anicich, V. G. 1993, *ApJ*, **84**, 215
- Aota, T., & Aikawa, Y. 2012, *ApJ*, **761**, 74
- Asplund, M., Grevesse, N., Sauval, A. J., & Scott, P. 2009, *ARA&A*, **47**, 481A
- Bohlin, R. C., Savage, B. D., & Drake, J. F. 1978, *ApJ*, **224**, 132
- Caux, E., Kahane, C., Castets, A., et al. 2011, *A&A*, **532A**, 23C
- Ceccarelli, C., Dominik, C., López-Sepulcre, A., et al. 2014, *ApJL*, **790**, L1
- Cernicharo, J., Decin, L., Barlow, M. J., et al. 2010, *A&A*, **518**, L136C
- Charnley, S. B., & Millar, T. J. 1994, *MNRAS*, **270**, 570C
- Codella, C., Ceccarelli, C., Bottinelli, S., et al. 2012, *ApJ*, **744**, 164
- Codella, C., Viti, S., Lefloch, B., et al. 2018, *MNRAS*, **474**, 5694C
- Cuadrado, S., Goicoechea, J. R., Pilleri, P., et al. 2015, *A&A*, **575A**, 82C
- De Beck, E., Kaminski, T., Patel, N. A., et al. 2013, *A&A*, **558A**, 132D
- Fontani, F., Ceccarelli, C., Favre, C., et al. 2017, *A&A*, **605A**, 57F
- Fontani, F., Rivilla, V. M., Caselli, P., et al. 2016, *ApJL*, **822**, L30
- Frerking, M. A., Langer, W. D., & Wilson, R. W. 1982, *ApJ*, **262**, 590
- Goicoechea, J. R., Pety, J., Gerin, M., Hily-Blant, P., & Le Bourlot, J. 2009, *A&A*, **498**, 771G
- Goto, M., Geballe, T. R., Indriolo, N., et al. 2014, *ApJ*, **786**, 96G
- Graedel, T. E., Langer, W. D., & Frerking, M. A. 1982, *ApJS*, **48**, 321G
- Halfen, D. T., Clouthier, D. J., & Ziurys, L. M. 2008, *ApJL*, **677**, L101H
- Harada, N., Herbst, E., & Wakelam, V. 2010, *ApJ*, **721**, 1570
- Harada, N., Riquelme, D., Viti, S., et al. 2015, *A&A*, **584A**, 102H
- Holdship, J., Viti, S., Jiménez-Serra, I., Makrymallis, A., & Priestley, F. 2017, *AJ*, **154**, 38H
- Jiménez-Serra, I., Caselli, P., Martín-Pintado, J., & Hartquist, T. W. 2008, *A&A*, **482**, 549J
- Jiménez-Serra, I., Vasyunin, A. I., Caselli, P., et al. 2016, *ApJL*, **830**, L6J
- Jura, M., & York, D. G. 1978, *ApJ*, **219**, 861
- Kaye, J. A., & Strobel, D. F. 1983, *GeoRL*, **10**, 957
- Koo, B.-C., Lee, Y.-H., Moon, D.-S., Yoon, S.-C., & Raymond, J. C. 2013, *Sci*, **342**, 1346
- Larson, H. P., Treffers, R. R., & Fink, U. 1977, *ApJ*, **211**, 972
- Lee, J. H., Michael, J. V., Payne, W. A., Whylock, D. A., & Stief, L. J. 1976, *JChPh*, **65**, 3280
- Lefloch, B., Vastel, C., Viti, S., et al. 2016, *MNRAS*, **462**, 3937L
- Lique, F., Jiménez-Serra, I., Viti, S., & Marinakis, S. 2018, *PCCP*, **20**, 5407L
- Maciá, E. 2005, *Chem Soc. Rev.*, **34**, 691
- MacKay, D. D. S., & Charnley, S. B. 2001, *MNRAS*, **325**, 545M
- McElroy, D., Walsh, C., Markwick, A. J., et al. 2013, *A&A*, **550A**, 36M
- Milam, S. N., Halfen, D. T., Tenenbaum, E. D., et al. 2008, *ApJ*, **684**, 618M
- Millar, T. J. 1991, *A&A*, **242**, 241M
- Mininni, C., Fontani, F., et al. 2018, *MNRAS*, **476**, L39
- Molinari, S., Brand, J., Cesaroni, R., & Palla, F. 2000, *A&A*, **355**, 617
- Morton, D. C. 1974, *ApJL*, **193**, L35M
- Neufeld, D. A., Wolfire, M. G., & Schilke, P. 2005, *ApJ*, **628**, 260N
- Pagani, L., Lesaffre, P., Roueff, E., et al. 2012, *RSPTA*, **370**, 5200
- Podio, L., Lefloch, B., Ceccarelli, C., Codella, C., & Bachiller, R. 2014, *A&A*, **565A**, 64P
- Quénard, D., Jiménez-Serra, I., Viti, S., Holdship, J., & Coutens, A. 2018, *MNRAS*, **474**, 2796
- Requena-Torres, M. A., Martín-Pintado, J., Rodríguez-Franco, A., et al. 2006, *A&A*, **455**, 971R
- Rivilla, V. M., Fontani, F., Beltrán, M. T., et al. 2016, *ApJ*, **826**, 161R
- Rivilla, V. M., Jiménez-Serra, I., Zeng, S., et al. 2018, *MNRAS*, **475**, L30
- Roberts, J. F., Rawlings, J. M. C., Viti, S., & Williams, D. A. 2007, *MNRAS*, **382**, 733R
- Schilke, P., Phillips, T. G., & Wang, N. 1995, *ApJ*, **441**, 334S
- Schilke, P., Pineau des Forêts, G., Walmsley, C. M., & Martín-Pintado, J. 2001, *A&A*, **372**, 291S
- Smith, D., McIntosh, B. J., & Adams, N. G. 1989, *JChPh*, **90**, 6213
- Tenenbaum, E. D., Woolf, N. J., & Ziurys, L. M. 2007, *ApJL*, **666**, L29T
- Tenenbaum, E. D., & Ziurys, L. M. 2008, *ApJL*, **680**, L121T
- Thorne, L. R., Anicich, V. G., & Huntress, W. T. 1983, *CPL*, **98**, 162
- Thorne, L. R., Anicich, V. G., Prasad, S. S., & Huntress, W. T., Jr. 1984, *ApJ*, **280**, 139
- Turner, B. E., Terzieva, R., & Herbst, E. 1999, *ApJ*, **518**, 699
- Turner, B. E., Tsuji, T., Bally, J., Guélin, M., & Cernicharo, J. 1990, *ApJ*, **365**, 569T
- Viti, S., Collings, M. P., Dever, J. W., McCoustra, M. R. S., & Williams, D. A. 2004, *MNRAS*, **354**, 1141V
- Viti, S., & Williams, D. A. 1999, *MNRAS*, **310**, 517V
- Wakelam, V., Loison, J.-C., Mereau, R., & Ruaud, M. 2017, *MolAs*, **6**, 22W
- Weisstein, E. W., & Serabyn, E. 1994, *Icar*, **109**, 367W
- Yamaguchi, T., Takano, S., Sakai, N., et al. 2011, *PASJ*, **63**, L37